PAPER

Check for updates

Durability and corrosion behaviors of superhydrophobic amorphous coatings: a contrastive investigation

Yunyun Ge,[a] Jiangbo Cheng, [ID] *[a] Lin Xue,[a] Baosen Zhang,[b] Peipei Zhang,[d] Xin Cui,[d] Sheng Hong,[a] Yuping Wu,[a] Xiancheng Zhang[c] and Xiubing Liang[d]

Superhydrophobic surfaces can be derived from roughening hydrophobic materials. However, the superhydrophobic surfaces with various micro/nano morphologies present variations of chemical and mechanical durability, which limits their practical applications. Very little actually is known about comparing durability and corrosion resistance of concave and convex superhydrophobic surface structures systematically. In this paper, two kinds of superhydrophobic AlNiTi amorphous coatings with concave and convex surfaces were obtained by chemical etching and hydrothermal methods, respectively. Benefiting from nanoscale sheet structure, the convex superhydrophobic coating displays higher water-repellence (contact angle = 157.6°), better self-cleaning performance and corrosion resistance. The corrosion current density of the convex superhydrophobic surface is approximately one order of magnitude smaller than the concave superhydrophobic surface. Besides, the long-term chemical stability and mechanical durability of both superhydrophobic surfaces were also investigated. The formation and damage mechanisms of these two kinds of superhydrophobic surfaces were proposed. It is hoped that these investigations could provide clear guidance for the real-world applications of superhydrophobic amorphous coatings.

1. Introduction

For the lotus leaf, there are hydrophobic wax tubules located on convex cell papillae on the surface, forming the hierarchically micro-nano structure. The micro-nano structure and hydrophobic molecules diminish the contact area of droplets with the surface, which leads to the formation and stability of air cushions.[1] It results in high contact angle (CA), low adhesive force and excellent self-cleaning properties.[2] Inspired by the lotus leaf effect, the superhydrophobic surface (water contact angle >150 °C) has generated widespread attention due to its excellent performance, for example, corrosion inhibition, self-cleaning and drag reduction, *etc.*[3–6] Meanwhile, the superhydrophobic characteristic also contains potential value in technical and industrial applications.[7]

The strategy for constructing superhydrophobic surfaces by using micro-nano structures and low surface energy materials is indispensable conditions.[8,9] Numerous methods have been successfully developed in the past few decades, such as anodic oxide,[10,11] chemical etching,[12–14] electrodeposition,[15,16] and hydrothermal method.[17–19] Among them, chemical etching and hydrothermal techniques are facile methods to prepare superhydrophobic coatings on metal surfaces. Chen *et al.*[12] designed a crater-like structured superhydrophobic Al alloy with HCl and stearic acid mixture solutions. The CA values of droplets all exceed 150° at different pH values, indicating the remarkable chemical and mechanical stability of the crater-like structure under acidic and alkaline conditions. Kumar *et al.*[13] reported that the superhydrophobic Al coating with rough rectangular pits-like microstructures was fabricated by chemical etching technique. The coating shows a high water static CA of 162.0° with excellent stability and self-cleaning performances. Guo *et al.*[14] synthesized superhydrophobic coating on a 7055-Al alloy surface with micron petal-shaped structures. The corrosion inhibition efficiency of the coating reaches 99.67%. The water repellency avoids the corrosion ions infiltrating the substrate and the growth of corrosion products. The superhydrophobic Al foils with a micro-nano sheet layer were fabricated using a one-step hydrothermal method.[17] The superhydrophobic surface shows drag reduction, self-cleaning and anti-icing properties. Zhang *et al.*[18] developed a one-step hydrothermal strategy to prepare superhydrophobic 5083-Al alloys with a high CA of 167.2°. The micro flower-like structures contribute to the

[a]College of Mechanics and Materials, Hohai University, Nanjing, 211100, P. R. China. E-mail: chengjiangbo@hotmail.com

[b]School of Materials Engineering, Nanjing Institute of Technology, Nanjing, 211167, P. R. China

[c]Key Laboratory of Pressure Systems and Safety, Ministry of Education, East China University of Science and Technology, Shanghai, 200237, P. R. China

[d]National Institute of Defense Technology Innovation, Academy of Military Sciences PLA China, Beijing, 100010, P. R. China

eventual anti-wetting performance and favorable corrosion resistance. An irregular conical structured superhydrophobic surface was formed on Al substrates by Lan *et al.*[19] The CA of the superhydrophobic surface reaches 162°, and the alloy exhibits a large charge transfer resistance (R_{ct}) and prominent anti-icing performances. To improve corrosion resistance of arc sprayed Al coating, the superhydrophobic surfaces with CA of 153.4° were obtained by ultrasonic etching and modification processing in our previous investigation.[20] The corrosion current density of superhydrophobic surface decreases by 2 orders of magnitude due to the formation of typical micro/nano-scale structures on the etched Al coating. The chemical and mechanical durability is a vital factor limiting superhydrophobic surfaces practical applications.[21] Though many recent advances in this region, the durability of superhydrophobic surface by different methods varies greatly. Nevertheless, extremely scarce reports concentrated on comparing corrosion resistance and durability of superhydrophobic surfaces prepared by etching and hydrothermal methods. It has remained elusive in micro-nano superhydrophobic structure of etched concave surface and hydrothermal convex surface. Therefore, it is highly desirable to clarify the corrosion resistance and durability of different micro/nanostructures superhydrophobic coatings.

Prompted by this, an attempt was initiated to synthesize two kinds of superhydrophobic structures on arc-sprayed AlNiTi amorphous coating surfaces by chemical etching and hydrothermal methods. The wettability and corrosion resistance of both superhydrophobic structures was compared. The chemical and mechanical durability were analyzed based on the liner friction and long-term corrosion experiments. Besides, the formation process and impairing mechanisms were further proposed.

2. Experimental procedures

2.1 Materials and chemicals

The substrates were commercial Q235 steel plates, and their chemical compositions were as follows: Fe of 98.96 wt%, C of 0.18 wt%, Mn of 0.60 wt%, Si of 0.22 wt%, S of 0.02 wt%, and P of 0.02 wt%. Trimethoxy (1H,1H,2H,2H-heptadecafluorodecyl) silane was supplied by Aladdin Chemical Reagent Co., LTD. (China). Sodium hydroxide, stearic acid, sodium chloride, hydrochloric acid, ethanol and acetone were bought from Chengdu Cologne Chemicals Co., LTD. (China). Colored chalks were purchased from Hubei Yingcheng Guangming Jinhua chalk Co., LTD. (China). The required chalk dust was obtained after grinding.

2.2 Synthesis of superhydrophobic AlNiTi amorphous coating

The self-developed cored wires made up of an Al sleeve that was filled with Ni and Ti alloy powders were used as spraying feedstock. The nominal composition of the cored wire was Al_{70}-$Ni_{20}Ti_{10}$ (at%). Q235 steel plates with size of 60 mm × 60 mm × 5 mm were selected as the substrate materials. The arc spraying process with a Laval nozzle gun was employed for the
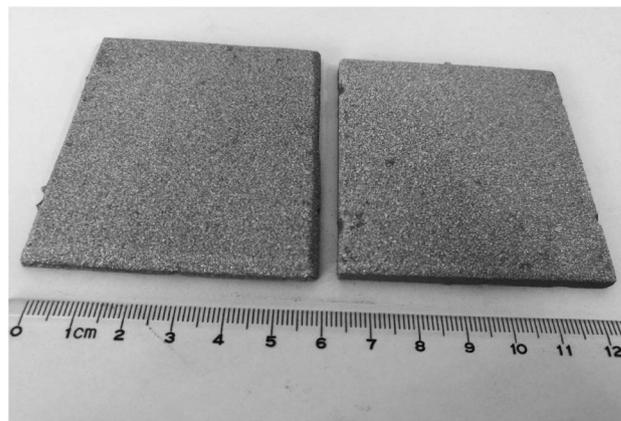

Fig. 1 The macroscopic images of the AlNiTi amorphous coatings.

preparation of the coating. The spraying parameters were as follows: spraying current 150 A, spraying voltage 34 V, stand-off distance 200 mm and compressed air pressure 700 kPa. The macroscopic images of the AlNiTi amorphous coatings were shown in Fig. 1. The coating has a high amorphous fraction of 85.9% and a denser structure with porosity up to 1%.[22]

The as-sprayed AlNiTi amorphous coating was denoted as the AS coating in the following. Firstly, the AS coating was ultrasonically cleaned with acetone, ethanol and deionized water for 10 min and then dried in air. The superhydrophobic AlNiTi amorphous coating was prepared by chemical etching and hydrothermal methods. The corresponding superhydrophobic coatings were named ES coating and HS coating, respectively. The preparation processes were schematically shown in Fig. 2. For the ES coating, the cleaned coating was chemically etched at 3 mol per L NaOH solution for 2 min. Afterward, the coating was instantly washed with ethanol and deionized water under sonication and dried. Next, at a stainless steel Teflon-lined autoclave of 50 mL capacity, the etched coating was immersed in 1% trimethoxy (1H,1H,2H,2H-heptadecafluorodecyl FAS-17) silane ethanol solution at 120 °C for 2 h and then dried at 110 °C for 0.5 h. As the HS coating, 0.1 g stearic acid was dissolved in 30 mL of 1 : 1 (v : v) ethanol/deionized water mixed solution to prepare the synthetic solution. Then the solution was transferred to a 50 mL stainless steel Teflon-lined autoclave. Subsequently, the washed coating was immersed in solution at 60 °C for 24 h and dried at 110 °C for 0.5 h.

2.3 Characterizations

The surface topography images of the coatings were observed by an environmental scanning electron microscope (Carl Zeiss Microscopy GmbH, 73447 Oberkochen, Germany). The roughness of the coatings was observed by a UP laser confocal microscope (RTEC, America). The chemical compositions were tested by X-ray photoelectron spectroscopy (XPS, ESCALAB 250Xi, Thermo Scientific) with Al Kα radiation. At room temperature, the CA of the coatings was determined with 3 µL of deionized water droplets by an OCA20 system coupled with
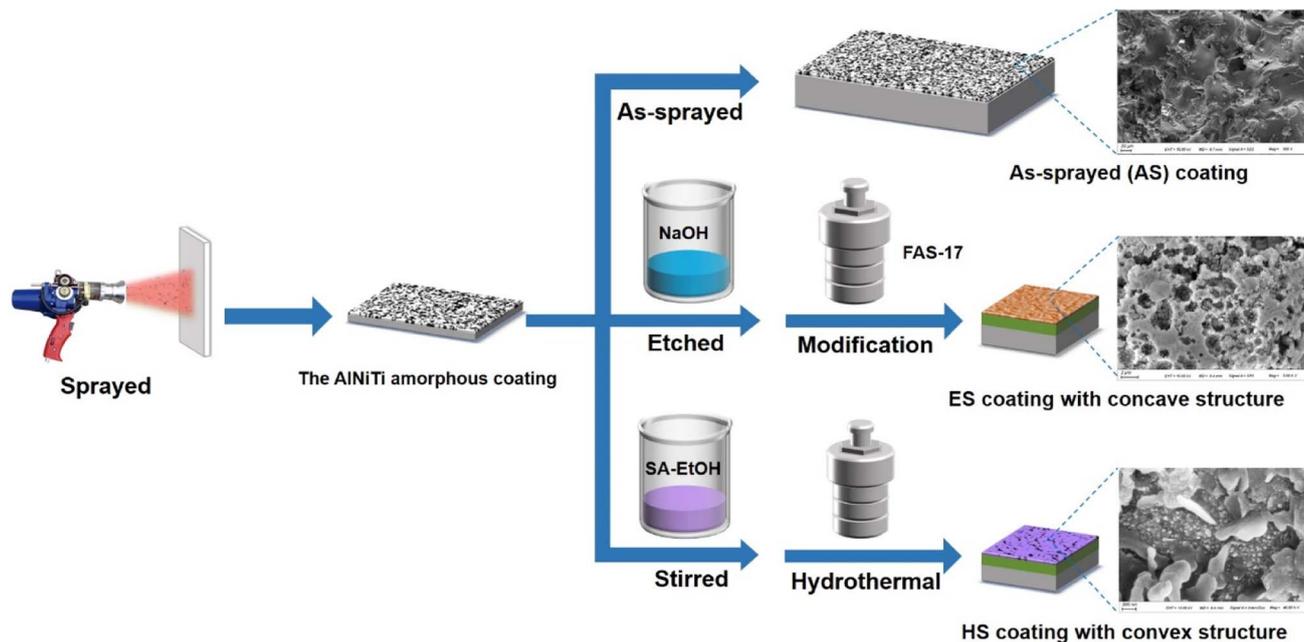
Fig. 2 Schematic diagram of preparation process for the coatings.

a CCD camera and SCA 20 software (Dataphysics GmbH, Germany) by a high-speed camera. The tests were measured at five random locations on the same sample to obtain the average CA values. A water drop was perpendicularly dropped on the coatings horizontally at 10 mm. The droplet bounce process was recorded with a high-speed camera to evaluate the water repellency of the coatings.

The electrochemical testing was determined to assess corrosion resistance of the coatings. The coatings were soaked in 3.5 wt% NaCl solution for 1 h at room temperature. The electrochemical work-station (CHI660D, Chen Hua Instruments Co., Ltd., China) was utilized to perform the potentiodynamic polarization and electrochemical impedance spectroscopy (EIS). The experiments were duplicated triple to realize repeatability. Deionized water droplets were vertically dropped onto the inclined coating surfaces of 10° covered with chalk ash to evaluate the self-cleaning performance of the coatings. The height of droplets was 2 cm from the coating surface. Simultaneously, the dirt removal process was recorded by a camera.

2.4 Measurements of durability

For the wettability measurement of liquids with pH values ranging from 1 to 14, droplets of 3 μL were deposited onto the as-sprayed, ES and HS coatings surface by a microsyringe. The long-term chemical durability of the coatings was further characterized by submersion in steady 0.1 mol per L HCl solution (pH = 1), 0.1 mol per L NaOH solution (pH = 13) and 3.5 wt% NaCl solution, respectively. The coatings were immersed in acid, alkaline and salt solutions for up to 24 hours, respectively. The changes in wettability of the coatings were measured by deionized water every 3–6 h.

Mechanical durability of the as-sprayed coating, the superhydrophobic ES and HS coatings were estimated by linear dry sandpaper-based abrasion. The coating surfaces were dragged on 800 mesh grit sandpapers at a speed of 5 cm s^{-1}, under a load of 100 g weight. The coatings (face to the sandpaper) were moved for 10 cm along the ruler and then moved back to the beginning along the ruler. This process is defined as one abrasion cycle. The water CA after each 50 cycles were tested by a contact angle measuring instrument (Theta flex, Biolin) using 10 μL droplets. The experiments were duplicated five times to realize repeatability.

3. Results

3.1 Surface micromorphology and water repellency

Fig. 3 shows the surface morphologies of the coatings. The AS coating displays a relatively smooth surface, as seen in Fig. 3(a) and (a1). The individual particle is a well-flattened splat and near disk-like shape. There is no evidence of extensive splashing particles. Numerous irregular micro-scale protrusions and a few micro-cracks are also detected on the surface. However, the surfaces of the ES and HS coatings are very rougher in comparison to the AS coating. The average surface roughness values of the AS, ES and HS coatings are 0.82 μm, 1.15 μm and 1.42 μm, respectively. After being etched by NaOH solution, many corrosion craters and irregular bulges are presented on the ES coating surface, as shown in Fig. 3(b) and (b1). The average size of corrosion pits is approximately 1.68 μm. As for the HS coating (Fig. 3(c) and (c1)), numerous micro/nanoscale hierarchical sheets with random distribution are unveiled on the surface. The thickness of these flake-like structures is range from 49 to 95 nm. Therefore, the etching and hydrothermal
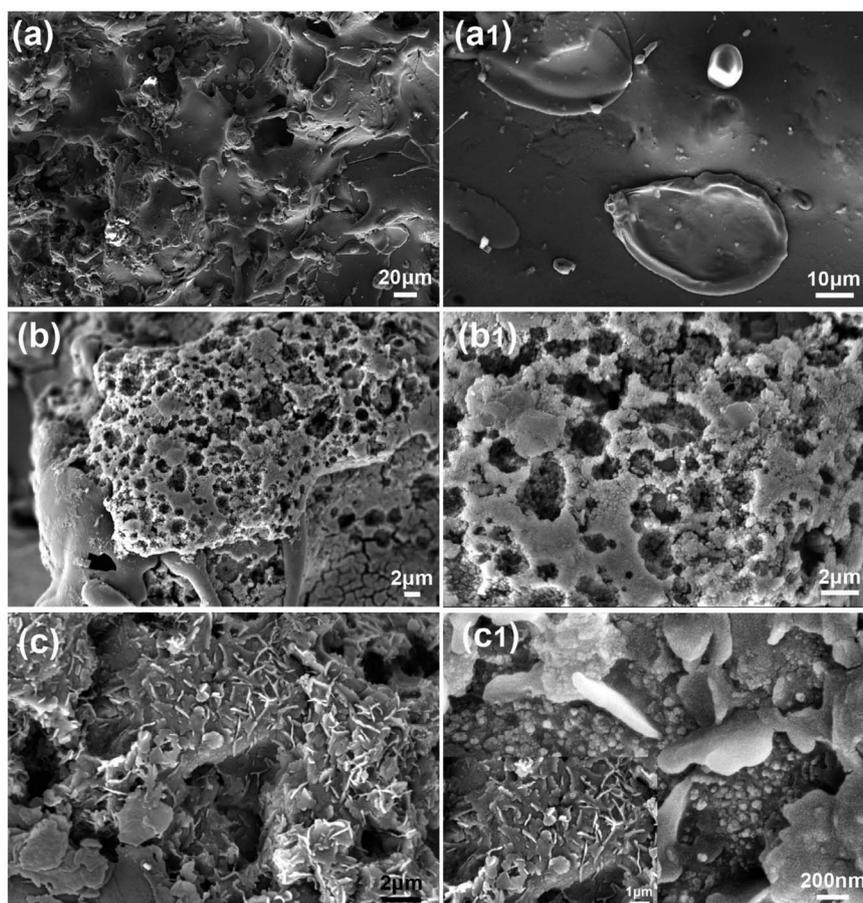
Fig. 3 SEM images of the AS coating (a) and (a1); the ES coating (b) and (b1); and the HS coating (c) and (c1).

processes promote the formation of micro/nanoscale hierarchical structures on the coating surfaces.

CA was used to evaluate the wetting performance of the coatings, as depicted in Fig. 4. The intrinsic wettability of the AS coating surface is 136.3°, indicating hydrophobic nature. Under chemical etching and FAS modification process, the prepared
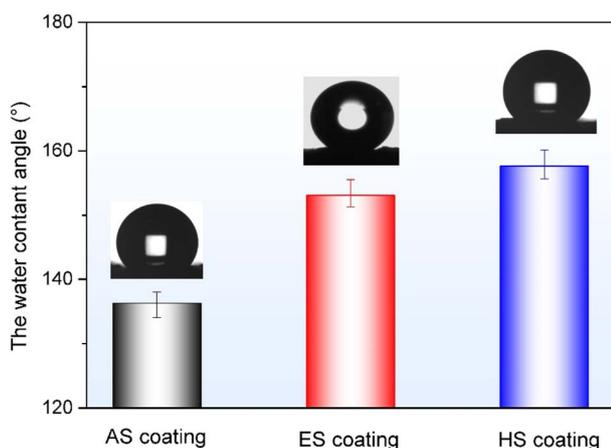
ES coating exhibits a typical superhydrophobic surface with a CA of 153.1°. Similarly, the superhydrophobic surface is also obtained on the HS coating with a CA value of 157.6°. The formation of the superhydrophobic surfaces is due to the retention of air pockets in the micro/nano hierarchical structures and the reduction of surface energy by chemical modification. Additionally, the HS coating surface shows stronger superhydrophobic properties than the ES coating surface. The reason is that the sheets formed on the hydrothermal convex surface are smaller micro/nano hierarchical structures than the corrosion pits on the etched concave surface.

Fig. 5 is the dynamic droplet impact process of the coatings. There are four states in drop bouncing experiments: no rebounds (deposition), partially bounce, completely bounces and fragments.[23] For the hydrophobic AS coating surface, under self-gravity, droplet drops vertically and strikes the coating surfaces. The droplet reaches its maximum deformation at 8 ms, as shown in Fig. 5(a). Subsequently, the droplet adheres to the surface because of massive energy loss in the process of extension and contraction, indicating no rebound process. Fig. 5(b) shows the dynamic droplet-bouncing process of the ES coating. The droplet achieves the maximum deformation at 12 ms. At 20 ms, it basically separates from the surface, but the partial droplet still adheres to the coating surface. For the HS
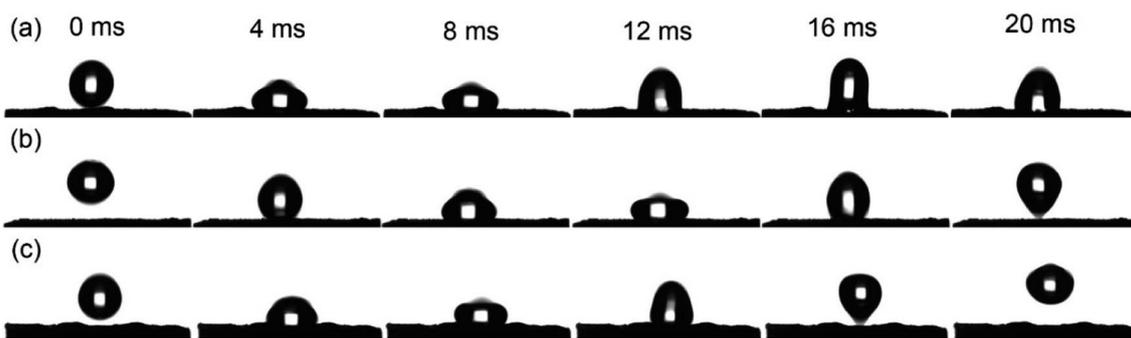

Fig. 4 CA values of the coatings.

Fig. 5 Sequence of snapshots of droplets (3 μL) impacting the coating surfaces: (a) the AS coating; (b) the ES coating; and (c) the HS coating.

coating in Fig. 5(c), the droplet is observed to undergo a complete rebound and leaves the surface after ~20 ms from impact, confirming the extreme superhydrophobic. Compared with the ES coating, the HS coating has better water repellency.

3.2 Self-cleaning behaviors

In real-world applications, the coatings are easily contaminated by gritty dirt. To mimic real pollution more closely, the chalk ash as contamination was selected to evaluate the self-cleaning performance of the prepared coatings. For the AS coating in Fig. 6(a), the chalk ash is wet by the water drops and significantly adhered to the surface. Though the droplets can take away the chalk ash from the ES coating surface, some partial contaminations still remain on the path of the droplets

movements (Fig. 6(b)). In contrast, supported by superior superhydrophobicity, water drops keep spherical and easily roll off from the HS coating surface, as shown in Fig. 6(c). In this process, the chalk ash is adhered to the surface of the water drop surface and then removed from the HS coating, forming a clean surface along the path of drop movement after only a few rolling cycles. Therefore, the HS coating displays a promising application of anti-adhesion and anti-fouling.

3.3 Corrosion resistance

Fig. 7(a) plots the potentiodynamic polarization curves of the coatings. The corrosion potential (E_{corr}) and corrosion current density (I_{corr}) are listed in Table 1. It can be seen that the AS coating shows the lowest E_{corr} of −0.762 V and the highest I_{corr}
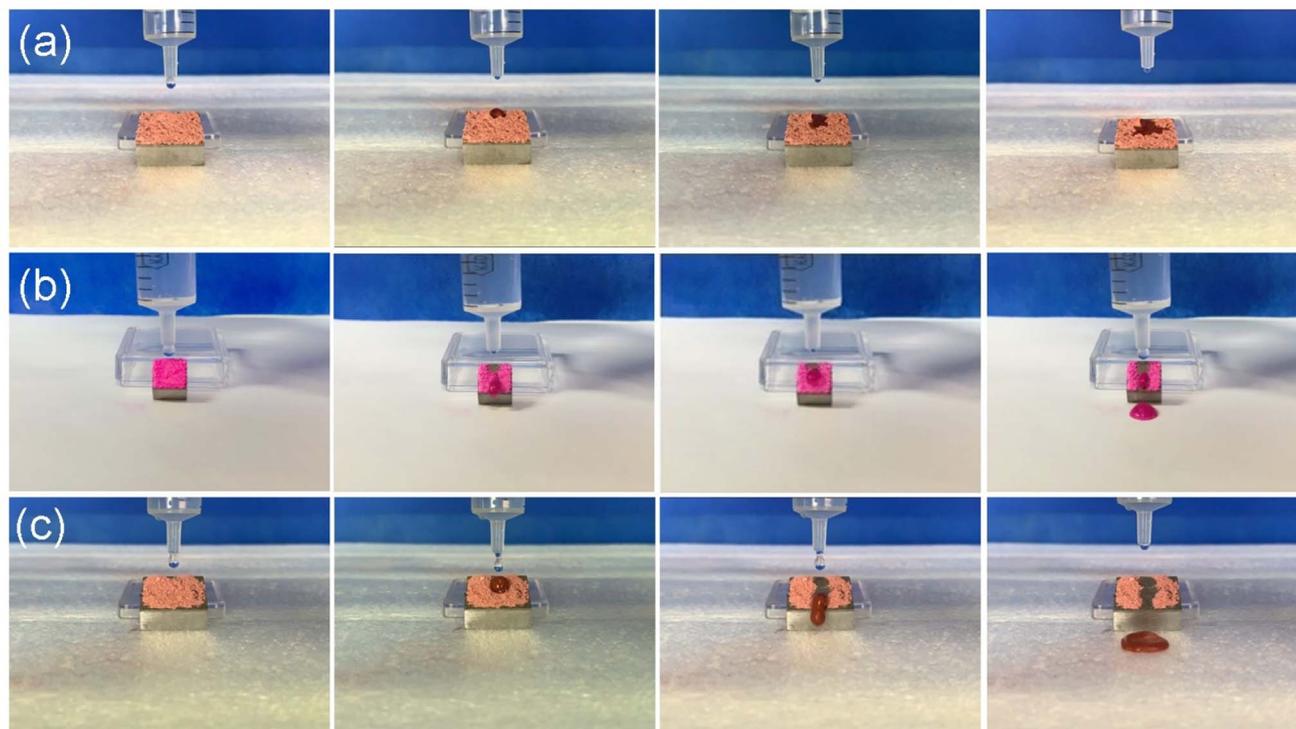

Fig. 6 Self-cleaning behaviors of the coatings (figure reference scale: the samples in a size of 10 mm × 10 mm × 7 mm): (a) the AS coating; (b) the ES coating; and (c) the HS coating.
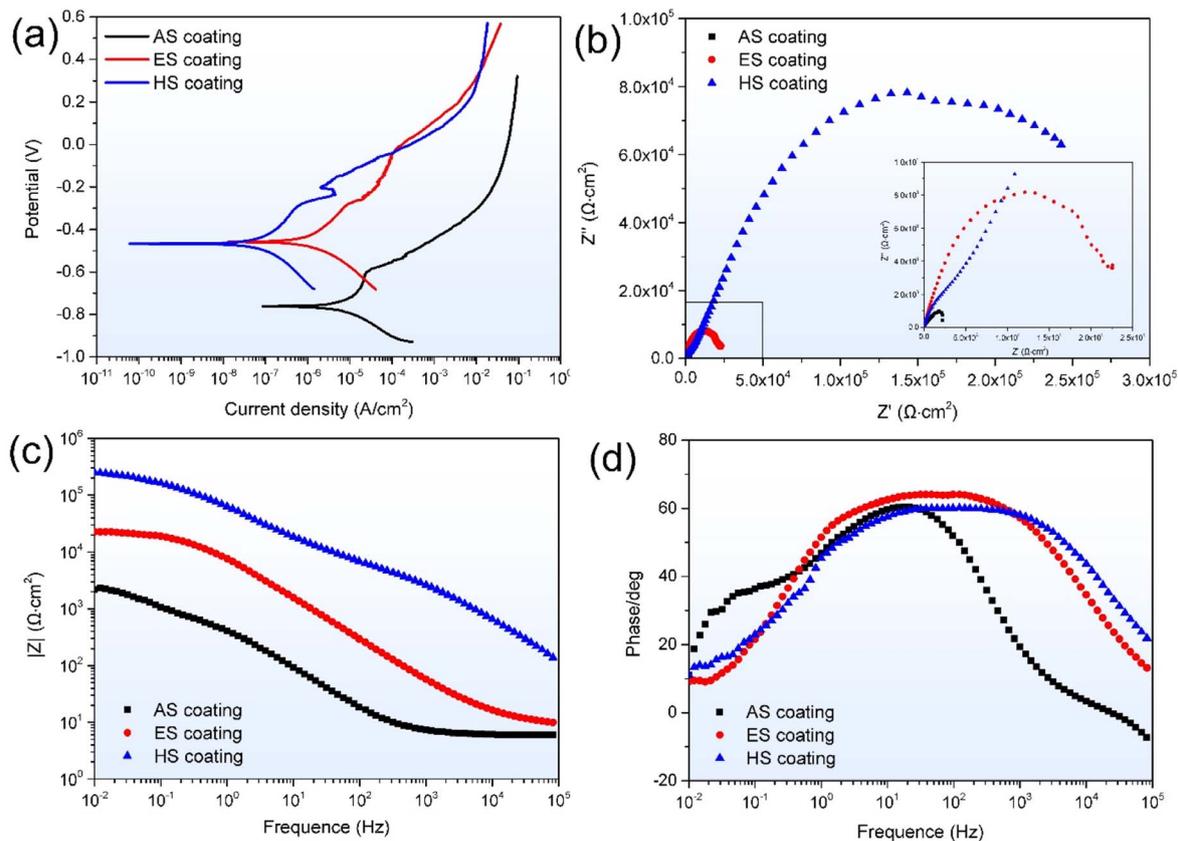
Fig. 7 (a) Potentiodynamic polarization curves, (b) Nyquist curves, (c) Bode modulus diagrams, and (d) Bode phase angle diagrams of the coatings.

Table 1 The electrochemical parameters of different coatings

Samples	E_{coor} (V)	I_{coor} (µA cm^{-2})	R_{p} (Ω cm^2)
The AS coating	−0.762	11.43	3491
The ES coating	−0.458	1.369	23267
The HS coating	−0.467	0.1032	360679

of 1.14×10^{-5} A cm^{-2}. For the superhydrophobic coatings, the E_{corr} values of the ES and HS coatings increase to −0.458 V and −0.467 V, respectively. The corresponding I_{corr} values significantly decrease to 1.37×10^{-6} A cm^{-2} and 1.03×10^{-7} A cm^{-2}, respectively. It is worth noting that the I_{corr} value of the HS coating is approximately two orders of magnitude lower than that of the AS coating and one order of magnitude smaller than that of the ES coating. Generally, the lower the I_{corr} value of the material, the better its corrosion resistance.[24] Consequently, the HS coating has excellent corrosion resistance in 3.5 wt% NaCl solution.

Fig. 7(b) illustrates the Nyquist plots of the coatings. Introducing the superhydrophobic surfaces causes a sharp increase in the diameter of the capacitive loops. In comparison to the ES superhydrophobic surface, the HS superhydrophobic surface displays a larger capacitive arc radius. The Bode modulus curves of the coatings are shown in Fig. 7(c). At a low frequency of

0.01 Hz, the impedance values of the AS and ES coatings are 2.21 and 22.79 kΩ cm^2, respectively. Similarly, the ES coating still has a higher impedance value of 9.94 Ω cm^2 than the AS coating of 6.02 Ω cm^2 at a high frequency of 10^5 Hz. Comparatively, the HS coating presents the maximum impedance values at both low-frequency and high-frequency stages. The values are 250.7 and 139.4 Ω cm^2, respectively. The larger impedance value and capacitive arc radius confirm the better corrosion resistance of the coatings.[24] Fig. 7(d) is the Bode phase angle diagrams of the coatings. All curves have the characteristic of a shoulder, as evidenced by two-time constants. The interaction between the electrolyte and the substrate produces a one-time constant at low frequencies. In the high-frequency region, it is due to the impedance provided by the amorphous coating or superhydrophobic surface. The phase angles of the ES and HS coatings are larger than the AS coatings, suggesting superior barrier performance and anticorrosion.

Fig. 8 presents the equivalent circuit ($R_s(Q_c(R_c(Q_{dl}(R_{ct}W))))$) to simulate the electrochemical processes of the coatings. In the circuit, R_s is the resistance of 3.5 wt% NaCl solution. Q_c and R_c are the constant phase element and resistance of the coating, respectively. Q_{dl} and R_{ct} represent double-layer capacitance and charge transfer resistance between the solution and the coating surfaces, respectively. W is Warburg impedance. The fitting
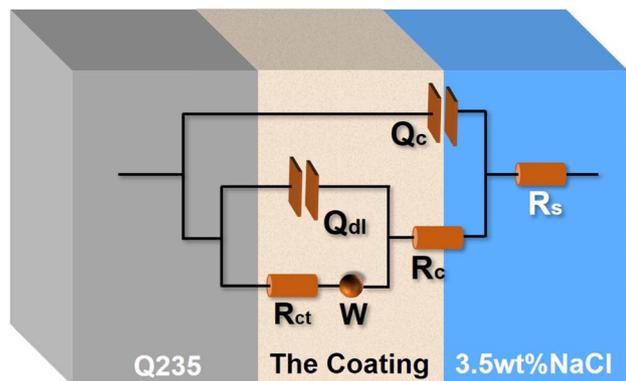
Fig. 8 Electrical equivalent circuits for EIS of the coatings: $R(Q(R(Q(RW))))$.

parameters are listed in Table 2. Generally, a low Q_{dl} and a high R_{ct} indicate a lower corrosion rate and better corrosion resistance.[25,26] From Table 2, Q_{dl} values of the AS, ES and HS coatings are 143.21×10^{-5}, 5.27×10^{-5} and 0.46×10^{-5} Ω^{-1} cm^{-2} s^{n}, respectively. It noted that Q_{dl} values of the ES and HS superhydrophobic coatings decrease two and three orders of magnitude that of the AS coating, respectively. Additionally, the AS coating presents a minimum R_{ct} value of 2.61 kΩ cm^2. The corresponding corrosion inhibition efficiency (η) of three coatings can be calculated by the equation:[27]

$$\eta\% = \frac{R_{ct}(S) - R_{ct}(A)}{R_{ct}(S)} \times 100 \quad (1)$$

where $R_{ct}(S)$ and $R_{ct}(A)$ are the charge transfer resistance of both superhydrophobic coatings and the as-sprayed coating, respectively. The HS coating has the maximum η value of 99.1% in 3.5 wt% NaCl solution, followed by the ES coating of 89.06%. Under the underpinning of the micro/nano hierarchical structure and the exceptional water repellency, the air film formed between the corrosion solution and the coating surface effectively retards the penetration of Cl$^-$ into the amorphous coating. Therefore, the corrosion resistance of the AlNiTi amorphous coating is improved significantly by superhydrophobic surface treatment.

3.4 Durability property

Durability is a critical parameter for superhydrophobic coatings in harsh natural conditions. Herein, the chemical stabilities of the coatings are tested by dripping droplets with different pH values onto the coating surfaces and measuring immediately

the CA values. The results are shown in Fig. 9(a). For the AS coating, the CA value does not change much in the range of pH 5–13. When the pH value is less than 5, it decreases slightly. The CA value decreases remarkably in alkaline solution (pH = 14). In contrast, the superhydrophobic surfaces have higher CA values than the AS coating. It shows a similar trend. When the pH value is less than or equal to 13, the CA values are essentially unchanged and all above 150°. In the solution of pH = 14, the CA value decreased significantly and the surfaces change from superhydrophobic to hydrophobic. Additionally, the HS coating has the highest CA values in all tests, indicating its good chemical stability.

Fig. 9(b)–(d) display the variations of CA values of the coatings in salt, acidic and alkaline electrolyte as a function of immersing time, respectively. As expected, the CA of the AS coating has a minimum value and decreases dramatically with the increase of immersing time. The surface nature transforms from hydrophobic surface to hydrophilic. Especially in NaOH solution, the CA value is about 1° after immersing for 6 h, as shown in Fig. 9(d). The slight decrease in CA values of the ES and HS coatings can be detected by long-term contact corrosive solutions. In NaCl and HCl solutions (Fig. 9(b) and (c)), the ES coating holds its superhydrophobicity up to 3 h, followed by a slight decrease to the hydrophobic surface with CA values of 141.7° and 140.2° after immersing 24 h, respectively. By contrast, even after soaking for 24 h in salt and acidic corrosive solutions, the CA value of the HS coating remains above 150°, indicating that the surface has excellent chemical stability. In alkaline conditions, the superhydrophobicity of the ES coating is quickly lost after immersion for 1 h, while the HS superhydrophobic surface can maintain up to 6 h. Even in this case, the ES and HS coatings at least hold their hydrophobicity for a relatively long time, as can be seen in Fig. 9(d). The above results reveal that the HS superhydrophobic surface can be used in various harsh environments, such as salt, acidic and alkaline conditions.

Besides being immersed in chemical solutions, sandpaper abrasion tests were also performed to validate the mechanical durability (Fig. 10(a)). As seen in Fig. 10(b), the contact angle of the AS coating surface decreases sharply from 136.3° to 111.4° after 350 cycles of abrasion. The CA values of the superhydrophobic surfaces decline marginally as a function of abrasion cycles. 200 cycles of abrasion would damage the micro/nano concave hierarchal structure on the ES coating surface and weaken water repellency with a CA of 149.8°. However, for the hydrothermal micro/nano hierarchal convex surface, the CA value still remains above 150° even after rubbing with

Table 2 The fitting circuit parameters for impedance spectra of different coatings

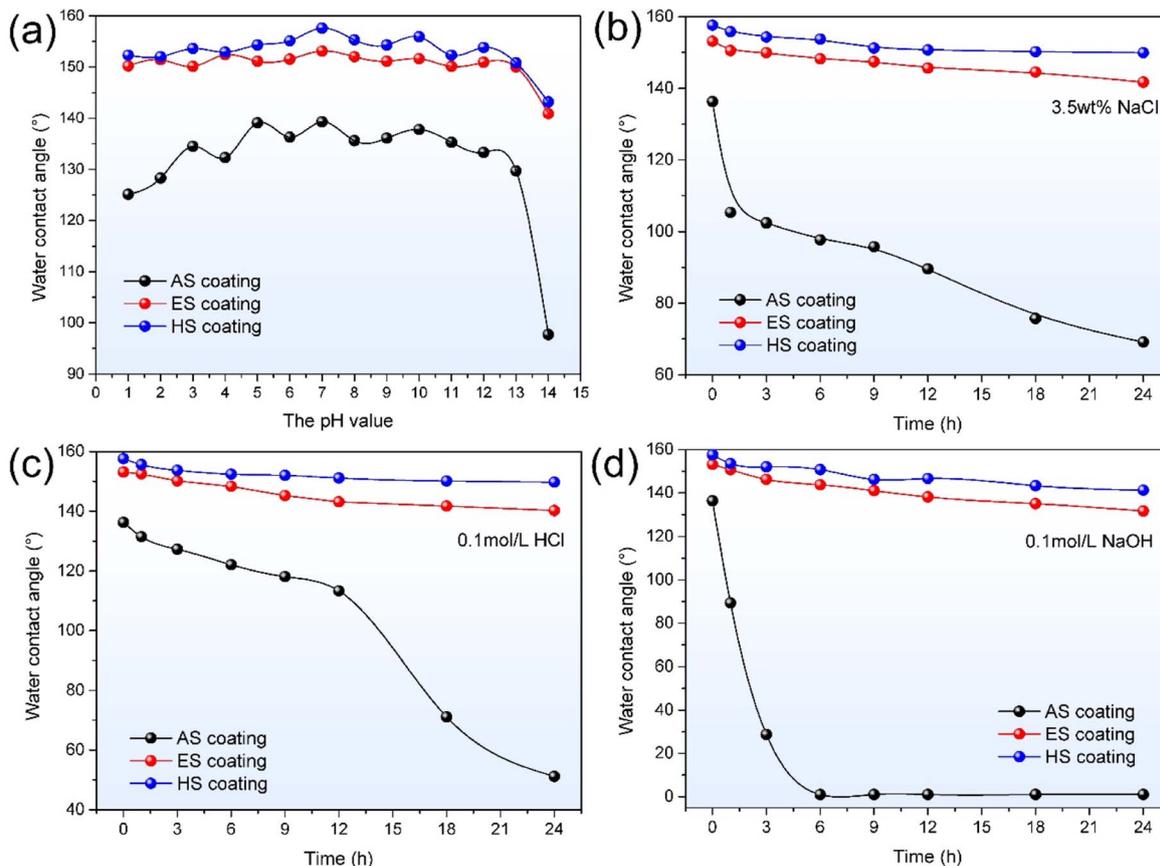| Samples	R_s (Ω cm^2)	$Q_c \times 10^{-5}$ (S cm^{-2} s^n)	n_c	R_c (Ω cm^2)	$Q_{dl} \times 10^{-5}$ (S cm^{-2} s^n)	n_{dl}	$R_{ct} \times 10^3$ (Ω cm^2)	W (S cm^{-2} s^5)	$\chi^2 \times 10^{-4}$
The AS coating	5.979	41.67	0.7791	754.6	143.2	0.6951	2.61	8.26×10^5	9.35
The ES coating	9.285	2.917	0.7379	0.012	5.269	0.8351	23.86	2.89×10^3	7.33
The HS coating	2.30×10^{-5}	0.035	0.7531	5129	0.456	0.5889	291.3	1.56×10^{-4}	1.20

Fig. 9 CA values of the coatings under different conditions of (a) droplets of different pH values; (b) 3.5 wt% NaCl solution; (c) 0.1 mol per L HCl solution; and (d) 0.1 mol per L NaOH solution.

sandpaper for 300 cycles. This is mainly due to the fact that the worn surface can still retain its micro/nano hierarchical structures, supplying the roughness necessary for super-hydrophobicity. After 350 cycles of abrasion, the CA values of the ES and HS coatings decrease to 144.6° and 147.2°, respectively. The high CA value demonstrates superior mechanical stability of the HS coating.

4. Discussions

4.1 Formation mechanism of the coatings

Chemical etching and hydrothermal methods are the simplest strategies to prepare superhydrophobic coatings. In this work, the ES coating is fabricated by a two-step process. Firstly, the AlNiTi amorphous coating is roughed with NaOH solution. Fig. 11(a) and (b) are SEM images and etching process
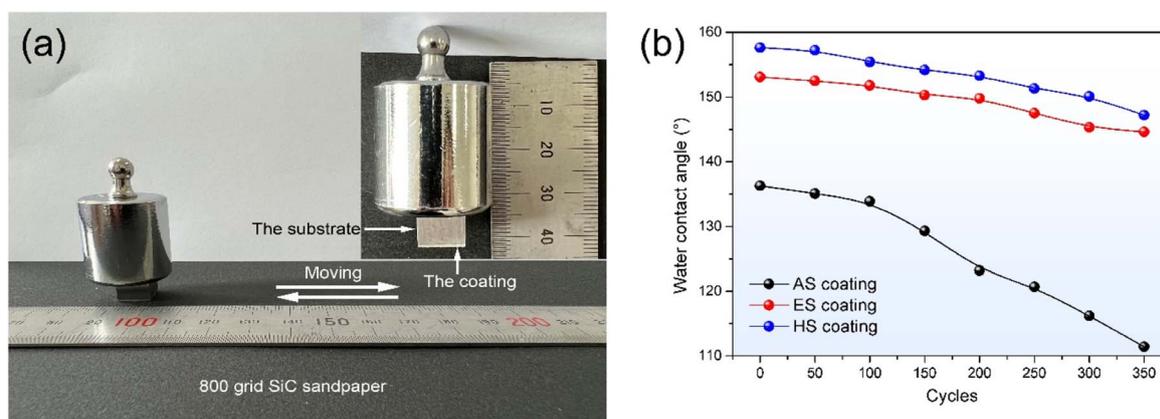

Fig. 10 (a) Schematic diagram of abrasion test and (b) CA values of the coatings after abrasion.
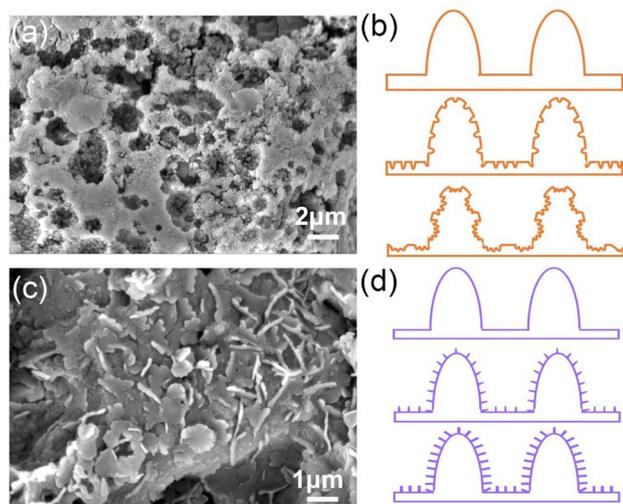
Fig. 11 (a) and (b) SEM image and etching process schematic diagrams of the ES coating; (c) and (d) SEM image and hydrothermal reaction process schematic diagrams of the HS coating.

schematic diagrams of the ES coating, respectively. At the initial stage of etching, corrosive pitting appears on the micro-protrusion surfaces, as seen in Fig. 11(b). As the etching progresses, the size of the pit increases gradually to a microscale corrosive crater, and then numerous nanoscale corrosion pits are formed inside them. It promotes the formation of micro/nanoscale hierarchical structures, which enhances the coating roughness. Secondly, the etched coatings are modified by trimethoxy (1H,1H,2H,2H-heptadecafluorodecyl) silane to reduce the surface energy.

After modification, the XPS spectra of the ES coating surface contain five elements: the F 1s at 689.1 eV, C 1s at 292.0 eV, O 1s at 532.8 eV, Si 2p at 104.1 eV and Al 2p at 74.8 eV, as shown in Fig. 12(a). The Al 2p spectrum consists of Al^{3+} (Fig. 12(b)), confirming the chemical reactions on the coating surface. For the C 1s spectrum in Fig. 12(c), all characteristic groups of trimethoxy (1H,1H,2H,2H-heptadecafluorodecyl) silane molecules are discovered including C–C at 285.3 eV, C–O at 286.5 eV, C–O–

Si at 288.9 eV, CF_2 at 291.7 eV and CF_3 at 293.9 eV. From Fig. 12(d), the peaks of Al–O at 530.8 eV and C–O at 532.9 eV are also remarked in the O 1s spectrum, respectively. The Al–O peak indicates that the low surface energy material trimethoxy (1H,1H,2H,2H-heptadecafluorodecyl) silane molecules are successfully grafted onto the coating surface through the formation of $Al[CF_3(CF_2)_7CH_2CH_2SiO]_3$. The reaction process is as follows:[18,28]

$$Al^{3+} + CF_3(CF_2)_7CH_2CH_2Si(OCH_2CH_3)_3 \rightarrow$$
$$Al[CF_3(CF_2)_7CH_2CH_2SiO]_3 \quad (2)$$

The CA value of the ES coating is up to 153.1°, as shown in Fig. 4. The superhydrophobicity and water repellent of the ES coating profit from ultralow surface energy groups of CF_2 and CF_3.

Fig. 11(d) shows the hydrothermal reaction process schematic diagrams of the HS coating. Numerous nanoscale sheet structures are formed on the coating surface by hydrothermal reaction. These nanoscale sheets grow gradually as a function of reaction time. Finally, the micro/nano hierarchical structures are formed and the surface roughness is improved, leading to its CA value of 157.6° (Fig. 3 and 4). Similarly, there are three signals of the C 1s (284.9 eV), O 1s (531.9 eV) and Al 2p (74.8 eV) on XPS spectra of the HS coating surface, as seen in Fig. 12(a). According to the illustration in Fig. 12(b), the high-resolution Al 2p consists of only one component Al^{3+} in the hydrolysis reaction. The peaks of high-resolution C 1s spectrum (Fig. 12(c)) at 284.4 eV, 284.8 eV and 288.5 eV correspond to C–C, C–O and O–C=O, respectively. There are two peaks of Al–O at 531.3 eV and C–O at 531.8 eV in high-resolution O 1s spectra (Fig. 12(d)). The presence of the Al–O peak indicates that the Branching reaction occurs on the coating surface:

$$Al^{3+} + CH_3(CH_2)_{16}COOH \rightarrow Al[CH_3(CH_2)_{16}COO]_3 \quad (3)$$
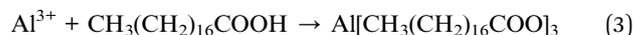
XPS results reveal the triumphant grafting of stearic acid on the surface. Therefore, the nanosheets are formed on the surface by hydrolysis of Al to Al^{3+} and neutralization reaction to
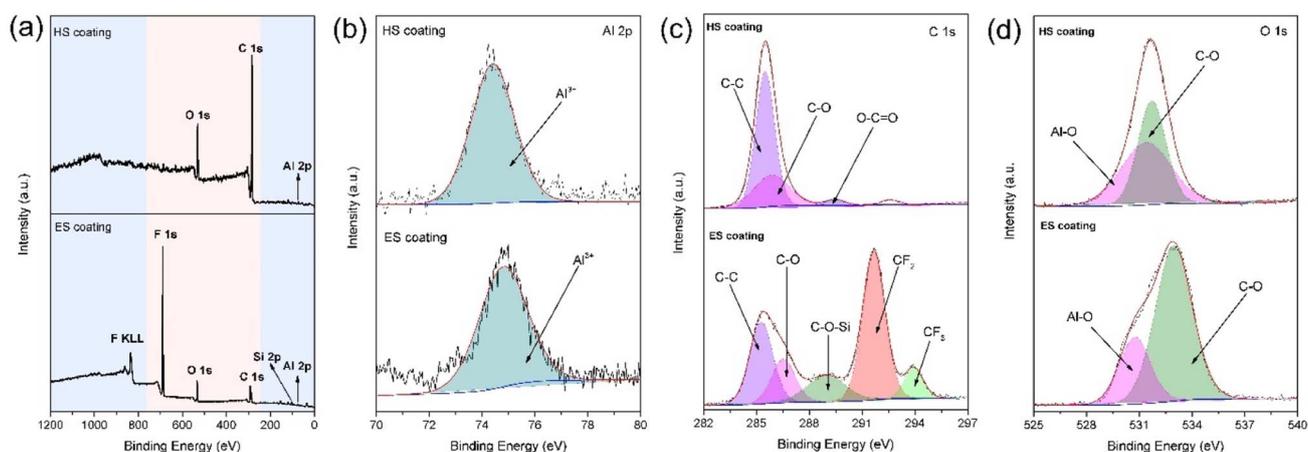

Fig. 12 XPS spectra of the ES and HS coatings: (a) survey spectra, (b) Al 2p, (c) C 1s, and (d) O 1s.

obtain $Al[CH_3(CH_2)_{16}COO]_3$ with low surface energy. Similar results were also reported for the superhydrophobic AA6061 alloys and superhydrophobic surfaces on aluminum foil.[17,29]

4.2 Durability mechanism of the coatings

From Fig. 7 and 9, the superhydrophobic coatings show better corrosion resistance in comparison to the AS coating. Furthermore, the HS coating presents long-term chemical durability. The improving mechanisms of chemical stability for the superhydrophobic coatings are illustrated by the model schematics diagrams, as shown in Fig. 13. For the AS coating surface, when water droplets drop on its surface, hydrophobic microscale Cassie state is formed due to numerous microscale protrusions. After being immersed in corrosive solutions, the coating surface is covered with a thin air film. The air film is easily destroyed under hydrostatic pressure, resulting in an irreversible transition from the microscale Cassie to the Wenzel state. As a result, the corrosive media (such as O_2, Cl^-, H^+ and OH^-) directly contact the coating surface and react with it.[30] With the extension of soaking time, corrosion media severely damage the coating surface and penetrates into the coating to form corrosion pits.

Based on the kinetic process of wetting transitions (WTs), the Cassie state will collapse when the pressure exceeds the critical pressure for the breakdown of the Cassie state.[31] For typical microscale pillar structures, the hydrophobic surface is derived from capillary pressure by the curvature of the droplets on the contact surface. Therefore, it is a crucial role to obtain a high critical pressure to resist further penetration of droplets by inducing nanostructure on the surface. For the ES coating, a large number of micro/nano corrosion pits are detected on the microscale protrusions surface by etching, as seen in Fig. 11(a). It leads to the transformation of microscale Cassie state to nanoscale Cassie state in corrosion solutions. The direct contact between corrosive media and the coating is inhibited by air cushions and closely spaced hydrophobic alkyl molecules. As corrosive media continuously erodes, some hydrophobic molecules will detach from the coating surface due to the partial decomposition of chemical interface bond. Subsequently, partial superhydrophobic film will be permeated by the formation of nano/micro pores and the coating surface will be wet. However, air pockets still exist in the structures. The ES coating shows an intermediate state, namely the Marmur state.[32] In this case, although the superhydrophobicity of the coating deteriorates, it still has excellent hydrophobicity in corrosive solutions, as shown in Fig. 9. For the HS coating, numerous nanoscale sheets exist on the micro-pillar surface, forming micro/nano hierarchical structures (Fig. 11(c) and (d)). Nano-Cassie state is triggered on the HS coating surface by droplets. Compared with micro-concave pits, the convex sheets have better superhydrophobic and durable properties due to their smaller size. This phenomenon can be explained by surface free energy curves, in which the interface of a stable solid–liquid–gas system needs to be convex rather than concave.[31,33]

The schematic diagrams of the mechanical durability mechanism for the coatings are depicted in Fig. 14. During the abrasion process, the micro protrusion parts at the top of the AS coating are easily worn under mechanical pressure (Fig. 14). The CA of the AS coating value decreases rapidly due to the reduction of roughness, as seen in Fig. 10(b). Comparatively, micro/nano hierarchical structures provide a valid method to strengthen the mechanical stability of superhydrophobic surfaces. In this case, the microstructures can bear the load and provide robustness to protect nanostructures. The remaining nanostructures ensure the superhydrophobicity of the coatings.[34] For the microscale concave structures, the micro/nano hierarchy is easily damaged by sandpaper, leading to the decrease of roughness and the removal of low-energy materials,
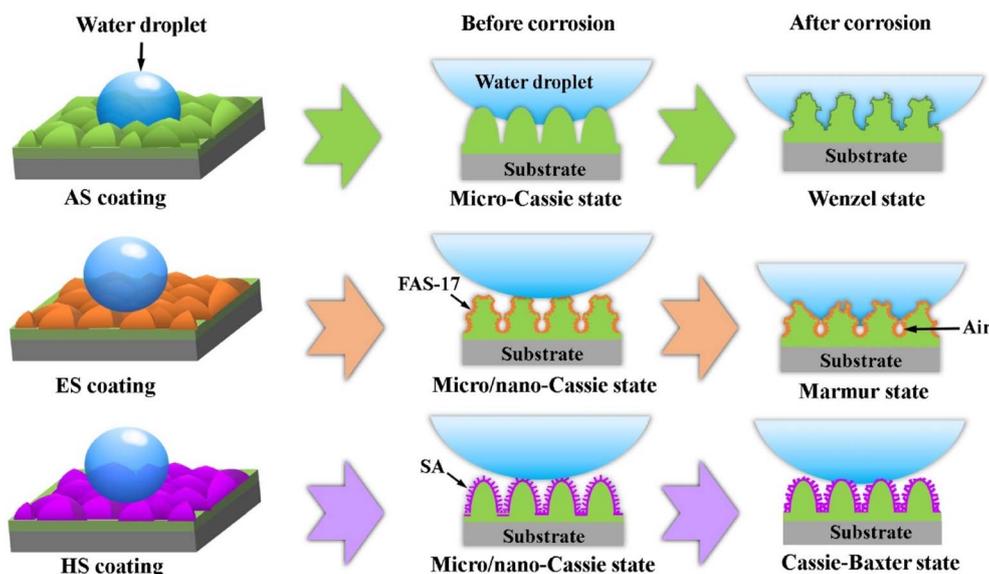

Fig. 13 Schematic diagrams of the chemical durability mechanisms for the coatings.
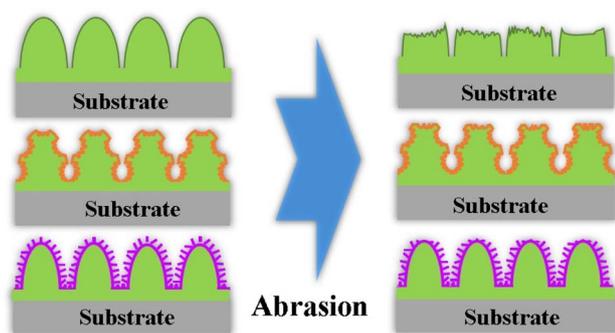
Fig. 14 Schematic diagrams of the mechanical durability mechanisms for the coatings.

thus worsening the superhydrophobic performance. However, the convex structures still hold the micro/nano hierarchical rough structures on their surfaces after abrasion. Hence, the nanoscale convex superhydrophobic surfaces have better mechanical durability.

The theory of energy thermodynamics can be used to reveal the superior chemical stability and durability of superhydrophobic surfaces with micro/nano convex structures. For the solid–liquid–air system, the surface free energy (W) is expressed as follows:[35]

$$W = A_{SL}\gamma_{SL} + A_{SA}\gamma_{SA} + A_{LA}\gamma_{LA} \qquad (4)$$

where A_{SL} and γ_{LA}, A_{SA} and γ_{SL} and A_{LA} and γ_{SA} are the areas and interfacial tensions of the solid/liquid interfaces, solid/air interfaces and liquid/air interfaces, respectively. To ensure the stability of the superhydrophobic surface, the local free energy needs to reach the minimum value, that is, $dW = 0$ and $d^2W > 0$. Through the Lagrange method including multiple variable constraints, the stability criterion formula is obtained as follows:[35]

$$dA_{SL}d\theta < 0 \qquad (5)$$

where $d\theta$ is a small change of local CA at the solid/liquid interface. In addition, it is also equal to the change in the slope of the surface. Consequently, the stability of the superhydrophobic surface depends on the sign of curvature, and a stable surface requires a convex surface, not a concave one.[35,36] Therefore, the prepared micro/nano convex surfaces possess excellent stable superhydrophobicity even after chemical or physical damage.

5. Conclusion

In this work, two kinds of superhydrophobic AlNiTi amorphous coatings were prepared by chemical etching and hydrothermal methods. Both coatings show typical micro/nano hierarchical structures: the concave pit structure with an average size of 1.68 μm for the ES coating and the convex sheets with a size range from 49 to 95 nm for the HS coating. The water contact angle value of the concave pit structure is 153.1°, while that of the convex sheet structure is 157.6°. Compared with the ES superhydrophobic coating, the HS superhydrophobic coating presents better water repellency, self-cleaning performance and corrosion resistance. The I_{corr} value of the HS coating is approximately two orders of magnitude lower than that of the AS coating and one order of magnitude smaller than that of the ES coating. The corrosion inhibition efficiency of the HS superhydrophobic coating reaches 99.1%. Additionally, the HS superhydrophobic coating shows better chemical durability under a harsh environment including long-term immersing in salt, acid and alkali solutions. Similarly, after 300 cycles of abrasion, the HS coating still remains superhydrophobicity, which is significantly higher than the 200 cycles of wear for the ES coating. The nano-convex superhydrophobic amorphous coating prepared by hydrothermal methods shows a promising application potential, due to its excellent self-cleaning, corrosion resistance, chemical and mechanical durability.

Conflicts of interest

There are no conflicts to declare.

Acknowledgements

References

1 C. Neinhuis and W. Barthlott, Characterization and distribution of water-repellent, self-cleaning plant surfaces, *Ann. Bot.*, 1997, **79**, 667–677.

2 X. F. Gao and L. Jiang, Water-repellent legs of water striders, *Nature*, 2004, **432**, 36–39.

3 B. Zhang, Q. Zhu, Y. Li and B. Hou, Facile fluorine-free one step fabrication of superhydrophobic aluminum surface towards self-cleaning and marine anticorrosion, *Chem. Eng. J.*, 2018, **352**, 625–633.

4 X. Bai, Y. Shen, H. Tian, Y. Yang, H. Feng and J. Li, Facile Fabrication of Superhydrophobic Wood Slice for Effective Water-in oil Emulsion Separation, *Sep. Purif. Technol.*, 2019, **210**, 402–408.

5 X. Gong, J. Zhang and S. Jiang, Ionic Liquid-induced Nanoporous Structures of Polymer Films, *Chem. Commun.*, 2020, **56**, 3054–3057.

6 Y. Ge, J. Cheng, X. Wang, L. Xue, S. Zhu, B. Zhang, S. Hong, Y. Wu, Xi. Zhang and X. Liang, Formation and Properties of Superhydrophobic Al Coatings on Steel, *ACS Omega*, 2021, **6**, 18383–18394.

7 X. Tian, T. Verho and R. H. A. Ras, Moving superhydrophobic surfaces toward real-world applications Standardized wear and durability testing is needed to advance the best materials, *Science*, 2016, **352**, 142–143.

8 F. Geyer, X. D'acunzi, A. Sharifi-Aghili, A. Saal, N. Gao, A. Kaltbeitzel, T. Sloot, R. Berger, H. Butt and D. Vollmer,

When and how self-cleaning of superhydrophobic surfaces works, *Sci. Adv.*, 2020, **6**, 9727–9737.

9 S. Li, K. Page, S. Sathasivam, F. Heale, G. He, Y. Lu, Y. Lai, G. Chen, C. J. Carmalt and I. P. Parkin, Efficiently texturing hierarchical superhydrophobic fluoride-free translucent films by AACVD with excellent durability and self-cleaning ability, *J. Mater. Chem. A*, 2018, **6**, 17633–17641.

10 V. S. Saji, Superhydrophobic surfaces and coatings by electrochemical anodic oxidation and plasma electrolytic oxidation, *Adv. Colloid Interface Sci.*, 2020, **283**, 102245.

11 D. Nakajima, T. Kikuchi, S. Natsui and R. O. Suzuki, Mirror-finished superhydrophobic aluminum surfaces modified by anodic alumina nanofibers and self-assembled monolayers, *Appl. Surf. Sci.*, 2018, **440**, 506–513.

12 C. Chen, S. Yang, L. Liu, H. Liu, L. Zhu and X. Xu, A green one-step fabrication of superhydrophobic metallic surfaces of aluminum and zinc, *J. Alloy Compd.*, 2017, **711**, 506–513.

13 A. Kumar and B. Gogoi, Development of durable self-cleaning superhydrophobic coatings for aluminium surfaces via chemical etching method, *Tribol. Int.*, 2018, **122**, 114–118.

14 F. Guo, S. Duan, D. Wu, K. Matsuda, T. Wang and Y. Zou, Facile etching fabrication of superhydrophobic 7055 aluminum alloy surface towards chloride environment anticorrosion, *Corros. Sci.*, 2021, **182**, 109262.

15 T. P. Rasitha, S. C. Vanithakumari, R. P. George and J. Philip, Template-Free One-Step Electrodeposition Method for Fabrication of Robust Superhydrophobic Coating on Ferritic Steel with Self-Cleaning Ability and Superior Corrosion Resistance, *Langmuir*, 2019, **35**, 12665–12679.

16 B. Zhang, X. Zhao, Y. Li and B. Hou, Fabrication of durable anticorrosion superhydrophobic surfaces on aluminum substrates via a facile one-step electrodeposition approach, *RSC Adv.*, 2016, **6**, 35455–35465.

17 Y. Tuo, W. Chen, H. Zhang, P. Li and X. Liu, One-step hydrothermal method to fabricate drag reduction superhydrophobic surface on aluminum foil, *Appl. Surf. Sci.*, 2018, **446**, 230–235.

18 B. Zhang, J. Wang and J. Zhang, Bioinspired one step hydrothermal fabricated superhydrophobic aluminum alloy with favorable corrosion resistance, *Colloids Surf., A*, 2020, **589**, 124469.

19 X. Lan, B. Zhang, J. Wang, X. Fan and J. Zhang, Hydrothermally structured superhydrophobic surface with superior anti-corrosion, anti-bacterial and anti-icing behaviors, *Colloids Surf., A*, 2021, **624**, 126820.

20 G. Wang, S. Liu, S. Wei, Y. Liu, J. Lian and Q. Jiang, Robust superhydrophobic surface on Al substrate with durability, corrosion resistance and ice-phobicity, *Sci. Rep.*, 2016, **6**, 20933–20942.

21 D. Wang, Q. Sun, M. J. Hokkanen, C. Zhang, F. Lin, Q. Liu, S. Zhu, T. Zhou, Q. Chang, B. He, Q. Zhou, L. Chen, Z. Wang, R. H. A. Ras and X. Deng, Design of robust superhydrophobic surfaces, *Nature*, 2020, **582**, 52–59.

22 J. Cheng, Y. Feng, C. Yan, X. Hu, R. Li and X. Liang, Development and Characterization of Al-Based Amorphous Coating, *JOM*, 2020, **72**, 745–753.

23 W. Li, Y. Lei, R. Chen, X. Zhu, Q. Liao, D. Ye and D. Li, Light caused droplet bouncing from a cavity-trap assisted superhydrophobic surface, *Langmuir*, 2020, **36**, 11068–11078.

24 K. Jüttner, Electrochemical impedance spectroscopy (EIS) of corrosion processes on inhomogeneous surfaces, *Electrochim. Acta*, 1990, **35**, 1501–1508.

25 C. Wu, Q. Liu, J. Liu, R. Chen, K. Takahashi, L. Liu, R. Li, P. Liu and J. Wang, Hierarchical flower like double-layer superhydrophobic films fabricated on AZ31 for corrosion protection and self-cleaning, *New J. Chem.*, 2017, **41**, 12767–12776.

26 L. Zheng, R. Shafack, B. Walker and K. Chan, The impact of high humidity on the ice-phobicity of copper-based superhydrophobic surfaces, *Nanomater. Nanotechnol.*, 2017, **7**, 1–6.

27 Z. Zhang, Z. Li, Z. Yu, S. Singh and C. Guo, Superhydrophobic Al Surfaces with Properties of Anticorrosion and Reparability, *ACS Omega*, 2018, **3**, 17425–17429.

28 P. Rodi, B. Kapun and I. Milošev, Superhydrophobic Aluminium Surface to Enhance Corrosion Resistance and Obtain Self-Cleaning and Anti-Icing Ability, *Molecules*, 2022, **27**, 1099–1118.

29 F. Wang and Z. Guo, Insitu growth of durable superhydrophobic Mg-Al layered double hydroxides nanoplatelets on aluminum alloys for corrosion resistance, *J. Alloy Compd.*, 2018, **767**, 382–391.

30 T. M. Mukhametkaliyev, M. A. Surmeneva, A. Vladescu, C. M. Cotrut, M. Braic, M. Dinu, M. D. Vranceanu, I. Pana, M. Mueller and R. A. Surmenev, A biodegradable AZ91 magnesium alloy coated with a thin nanostructured hydroxyapatite for improving the corrosion resistance, *Mater. Sci. Eng. Carbon*, 2017, **75**, 95–103.

31 W. Zhang, D. Wang, Z. Sun, J. Song and X. Deng, Robust superhydrophobicity: mechanisms and strategies, *Chem. Soc. Rev.*, 2021, **50**, 4031–4061.

32 A. Marmur, Wetting on Hydrophobic Rough Surfaces: To Be Heterogeneous or Not To Be?, *Langmuir*, 2003, **19**, 8343–8348.

33 B. Bhushan and Y. C. Jung, Natural and biomimetic artificial surfaces for superhydrophobicity, self-cleaning, low adhesion, and drag reduction, *Prog. Mater. Sci.*, 2011, **56**, 1–108.

34 T. Verho, C. Bower, P. Andrew, S. Franssila, O. Ikkala and R. H. Ras, Mechanically Durable Superhydrophobic Surfaces, *Adv. Mater.*, 2011, **23**, 673–678.

35 M. Nosonovsky, Multiscale Roughness and Stability of Superhydrophobic Biomimetic Interfaces, *Langmuir*, 2007, **23**, 3157–3161.

36 Y. Sia and Z. Guo, Superhydrophobic nanocoatings: from materials to fabrications and to applications, *Nanoscale*, 2015, **7**, 5922–5946.